ACS Photonics

Article

pubs.acs.org/journal/apchd5

Octupolar Plasmonic Meta-Molecules for Nonlinear Chiral Watermarking at Subwavelength Scale

Radoslaw Kolkowski,*[†,‡] Lucia Petti,[§] Massimo Rippa,[§] Clement Lafargue,[†] and Joseph Zyss[†,§]

[†]Laboratoire de Photonique Quantique et Moléculaire (LPQM), École Normale Supérieure de Cachan, 61 Avenue du Président Wilson, 94230 Cachan, France

[‡]Advanced Materials Engineering and Modelling Group, Faculty of Chemistry, Wroclaw University of Technology, Wybrzeze Wyspianskiego 27, 50-370 Wroclaw, Poland

[§]Institute of Applied Sciences and Intelligent Systems - ISASI, CNR, Via Campi Flegrei, 34 - Comprensorio Olivetti, 80078 Pozzuoli (Napoli), Italy

Supporting Information

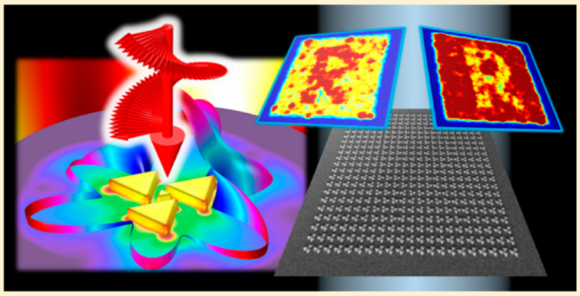

ABSTRACT: Nonlinear chiroptical effects of precisely designed chiral plasmonic nanomaterials can be much stronger than such effects observed in the linear regime. We take advantage of this property to demonstrate the use of circularly polarized second-harmonic generation microscopy toward the efficient read-out of a microscopic pattern encoded by an array of triangular gold nanoprisms forming arrangements of adequate chiral symmetry. Strong chiroptical effects are observed in the backscattered second-harmonic generation intensity, enabling clear distinction of the laterally arranged enantiomers, down to nearly 1 μm resolution, with an overall intensity contrast of about 40% (second-harmonic generation circular dichroism of 20%). Numerical simulations show a noticeable change in the spatial distribution of plasmonic hot spots within the individual nanostructures under excitation by circularly polarized light of different handedness. This leads to rather weak chiroptical effect in the linear backscattering (theoretical circular dichroism not exceeding 3%), in contrast with the much more significant change of the second-harmonic generation in the far-field (second-harmonic generation circular dichroism from 16 up to 37%). These results open the possibility of designing deeply subwavelength chiral nanostructures for encoding microscopic “watermarks”, which cannot be easily accessed by linear optical methods, moreover requiring a nonlinear microscopy setup for reading out the encoded pattern.

KEYWORDS: *second-harmonic generation, chiral plasmonic nanostructures, meta-molecules, circular dichroism, gold nanoprisms, nonlinear microscopy*

Over the past two decades, research devoted to the second-harmonic generation (SHG) from plasmonic nanostructures evolved from the investigation of hyper-Rayleigh scattering in colloidal suspensions of metal nanoparticles[1−3] toward the measurements of SHG from individual plasmonic nano-objects.[4−6] Far-field SHG radiation pattern has been demonstrated as a highly sensitive probe of the nanoscale optical field distribution,[7] allowing for the investigation of multipolar plasmon modes,[8−10] the analysis of surface plasmon polariton (SPP)-mediated interactions,[11,12] refractive index sensing,[13] and precise characterization of the nanostructure geometry.[14−16] In parallel, advanced theoretical tools for SHG modeling were developed, based on numerical methods such as finite elements to solve Maxwell equations and yield the scattered SHG radiation.[17−19] Among the geometrical properties that can be addressed by SHG microscopy, chirality stands out as one of the most interesting probes of light−matter interactions, especially in the context of chiral plasmonic meta-materials, which have been reported to exhibit giant optical activity in the linear regime.[20,21] Valev et al. have thus reported extensive work on chirality in SHG from specially patterned superchiral meta-surfaces.[7,22−24] The location of plasmonic hot spots and their influence on the chiroptical response have been thoroughly addressed,[22,23] leading to reports of nonlinear chiroptical effects reaching magnitudes as high as 52%.[24] However, the basic building blocks of the investigated meta-materials were relatively large, with lateral sizes of the order of 1 μm, which is not compatible with the encoding of chirality-based information below the typical diffraction limit of SHG microscopy. Recently, many sophisticated fabrication techniques were developed, including optical vortex laser ablation,[25] DNA-assisted self-assembly of plasmonic nanoparticles,[26] focused ion and electron beam assisted deposition,[27] or hole-mask lithography combined with tilted angle evaporation,[28] enabling creation of deeply subwavelength 3D helicoidal metal nanostructures exhibiting strong chiroptical effects in their

Received: February 27, 2015
Published: June 12, 2015

DOI: 10.1021/acsphotonics.5b00090
ACS Photonics 2015, 2, 899−906

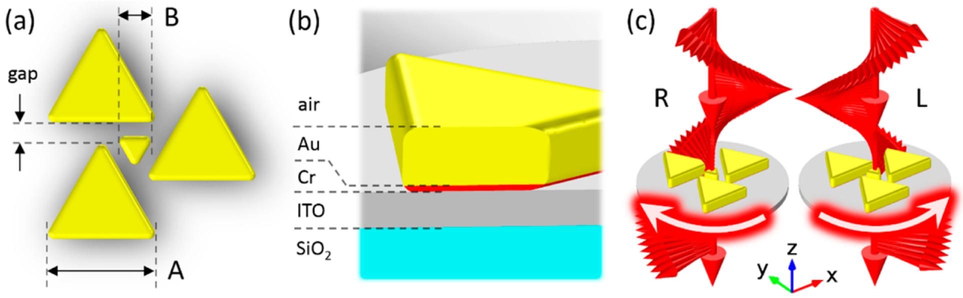

Figure 1. Geometry of the investigated nanostructures: (a) three parameters defining the lateral geometry, presented on the example of the left-enantiomer: $A \approx 200$ nm, side length of the gold nanoprisms, $B \approx 60$ nm, side length of the smaller central gold nanoprism (referred to as "central nanoparticle"), and the gap in-between nanoprisms equal around 40 nm; (b) cross-section of the sample, showing its layered structure: SiO_2 substrate (blue), ITO layer (25 nm, gray), chromium adhesion layer (3 nm, red), and gold nanostructure (40 nm, yellow), surrounded by air; (c) excitation configuration, showing the applied convention for defining the particular handedness (left of right) of the incident light. The images were exported from a COMSOL Multiphysics software and correspond to the numerically modeled geometry.

linear optical response. However, the nonlinear chiroptical behavior of these nanostructures, potentially extremely high, remains to be explored.

In this work, we demonstrate a strong chiroptical effect in second-harmonic generation from simple 2D chiral arrangements of gold nanostructures fabricated by means of electron beam lithography (EBL). Our nanostructures are composed of four gold nanoparticles: three gold nanoprisms arranged into a "pinwheel" and a smaller gold nanoparticle in the center. The structure and composition of our samples are presented in the Figure 1a and b, respectively. Indeed, this blueprint is characterized by 3-fold symmetry, where chirality is further introduced by removing the three mirror planes starting from the three apex of the nanoprism. Such symmetry lowering from a high symmetry equilateral triangle, is obtained by adequate mutual organization of the nanoprisms that lowers the symmetry from $C3v$ to $C3$, while ensuring interactions between them. Such nanoscale engineering can be viewed, in terms of symmetry, as the up-scaling of the earlier chiral octupolar molecule concept,[29,30] into the realm and scale of metamaterials, leading us to consider such interacting and plasmon sustaining nanoentities as "meta-molecules". Here, the term "octupolar" refers to the 3-fold symmetry and the related rotational properties of the quadratic susceptibility tensor that behaves under rotations as an octupolar charge distribution tensor,[30] and should not be confused with the multipolar oscillation modes, often mentioned in the context of plasmonic nanoparticles.[31] A first theoretical investigation of such octupolar meta-molecule blueprints in 2- and 3-D had pointed-out the potentially high nonlinearity of such entities[32] but did not consider the further implementation of chiral features therein. On the other hand, chiral plasmonic meta-molecules have recently been investigated by means of optical transmission measurements, showing noticeable circular dichroism in the linear regime.[33,34] A smaller nanoparticle at the center of the structure is intended to play different roles. First, it demonstrates an implementation of the plasmonic nanolens concept,[35] one of the successful strategies proposed for improving the SHG scattering efficiency. Second, the nanoparticle is located at a position where the local electric field enhancement is presumed to dramatically change under different handedness of incident light polarization. Hence, this central nanoparticle is expected to act as a near-field nonlinear nanoprobe, giving rise to a significant enhancement of the overall nonlinear chiroptical response of the nanostructure.

We investigate two enantiomers, chiral arrangements being the mirror images of each other, further referred to as left- and right-enantiomer based on their different SHG responses under circularly polarized incident light. By convention, we will call a left-enantiomer the entity that emits a more intense SH under left-handed circularly polarized excitation and vice versa for the right-enantiomer. The sample is irradiated by normally incident circularly polarized light, with either right (R, clockwise) or left (L, anticlockwise) handedness, defined according to the convention: $\mathbf{E}_L = (1,-i)\exp(ikz + i\omega t)$ and $\mathbf{E}_R = (1,+i)\exp(ikz + i\omega t)$ (with propagation direction toward $-z$), as illustrated in Figure 1c (the convention for handedness is chosen as seen from the source). All components of the nanostructure are following an equilateral triangle template, thus, displaying a noncentrosymmetric shape. Whereas such a symmetry condition is not applying strictly speaking to quadratic nonlinearities when sustained by nonlocal plasmonic excitations, a noncentrosymetric shape is known to enhance the efficiency of the process, as shown in ref 6, where triangular entities were shown to be more efficient than rectangles by 1 order of magnitude, thereby providing a sound starting basis toward further introduction of chiral features. In the absence of such features for individual triangular nanoparticles, the observed chirality can only originate from near-field plasmonic interactions that bond the nonchiral nanoparticles into a single 2D chiral entity. As a result, the locations of plasmonic hot spots strongly depend on the handedness of the incident light, causing strong chiroptical SHG response. Two enantiomers and a nonchiral reference, arranged in distinct 10 × 10 square arrays of "meta-molecules", are set together and compared in a single SHG imaging experiment. Additionally, we investigate arrays composed of the left-enantiomers, in which some are replaced by right-enantiomers, forming a microscopic pattern, further referred to as a "watermark", that can be efficiently read out using SHG scanning microscopy with a circularly polarized excitation beam. We compare the results of the nonlinear optical measurements with the UV−vis extinction spectra obtained on large arrays of nanostructures, showing that the linear chiroptical effect is much weaker than its SHG counterpart. This is confirmed by numerical finite element-based simulations, performed at both fundamental and second-harmonic frequencies, revealing the peculiar mechanism of the chiroptical response of these nanostructures.

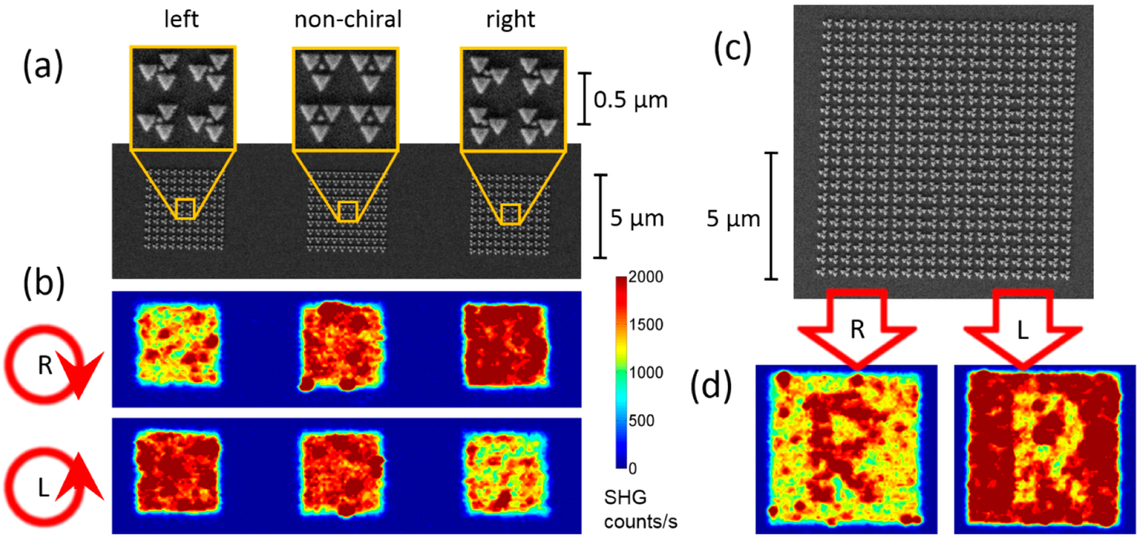

Figure 2. (a) SEM image of the three uniform arrays, composed of left-enantiomers (on the left), nonchiral reference nanostructures (in the middle), and right-enantiomers (on the right); (b) SHG scanning microscopy images of the three arrays, obtained under excitation at fundamental wavelength 850 nm with R (top) and L (bottom) circular polarization; (c) SEM image of the "watermark" formed by a mixture of right- and left-enantiomers; (d) SHG images of the "watermark" obtained with R and L polarization (as indicated). The SHG intensity scale in between (b) and (d) is common for all SHG images presented in the following figure.

RESULTS AND METHODS

SHG Microscopy. An inverted nonlinear optical microscopy configuration is used to detect the backscattered SHG emission from the investigated samples. A femtosecond laser beam at 850 nm emission wavelength is generated by a Spectra Physics Mai-Tai Ti:sapphire laser (100 fs, 80 MHz) to provide the fundamental excitation. The polarization of the incident light is precisely controlled by a tunable liquid crystalline phase retarder (Thorlabs) with the aid of a half-wave plate mounted on a motorized rotation stage. The two above elements are adjusted so that after further reflection from a dichroic mirror, the beam incident on the sample is either left-handed or right-handed circularly polarized, with an absolute ellipticity not exceeding 1%. Switching between the two polarization states is achieved by simply rotating the half-wave plate by 45° (from −22.5° to +22.5°) and can be performed with good repeatability after initial calibration. The average power of the beam at the entrance of the microscope is around 5 mW. The incident light is focused by an air objective of numerical aperture 0.7 and magnification 60× (Nikon). The same objective collects the backscattered SHG radiation at 425 nm, which is then transmitted through a dichroic mirror and a set of filters, and finally measured by a single photon counting avalanche photodiode (Laser Components GmbH). The SHG images are performed by scanning the xy sample position, by use of a piezoelectric translation stage (Piezojena), the measured SHG photon counts being recorded as a function of the sample displacement.

We began our investigation with 10 × 10 square arrays, each array composed of objects of the same well-defined handedness. The nanostructures were fabricated using top-down EBL technique, followed by gold deposition using e-beam evaporation technique (more details on fabrication are included in the SI). The lattice period is 500 nm, which is below the resolution limit of the objective used in the SHG experiment, and therefore the arrays appear in the SHG images as continuous bright areas. The pattern composed of three arrays (left-enantiomers, nonchiral nanostructures, and right-enantiomers) is shown in the SEM images in Figure 2a, and the images of this pattern obtained by SHG microscopy using a fundamental wavelength of 850 nm (SHG wavelength 425 nm) are presented in Figure 2b. The top image was obtained by excitation with the R polarization, whereas the bottom image was recorded using L polarization. The chiroptical effect is clearly seen in the changes of the recorded SHG intensity. Under R polarization, the average SHG signal from the right-enantiomer is significantly more intense than the signal from the left-enantiomer. This situation is reversed when the polarization is switched to L: this time the left-enantiomer produces more intense SHG, while the right-enantiomer appears much darker. In the same time, no significant changes in the SHG intensity are observed in the nonchiral reference array in the middle, when shining R- or L-polarized light.

Apart from the chiroptical effect, the SHG intensity distribution within an individual array is not uniform: very bright hot spots can be occasionally observed in some points for each array. We attribute these hot spots to undesired structural defects, such as surface roughness with sharp features[6] or nanoparticles getting in contact with each other. SEM images presenting examples of such defects can be found in the SI (together with a theoretical analysis of their influence on the nonlinear chiroptical response). These imperfections may result in large local field enhancements, affecting the SHG intensity detected from these areas. On the example of experimental results presented in Figure 2, the average signal is in the order of 1000−2500 cts/s (counts per second), but it can reach values from 4000 up to 12000 cts/s at the hot spots. Despite this inhomogeneity in the nonlinear response of our samples, their general chiroptical behavior appears clear-cut and repeatable. We have also proved that the measured SHG comes mainly from the nanostructures (Au surface, Cr surface and Cr-ITO interface), as the SHG signal from the bare substrate (air-ITO and ITO-glass interfaces) is at the level of a dark count rate.

In order to quantify the magnitude of nonlinear chiroptical effects, a parameter called SHG-circular dichroism (SHG-CD) has been proposed.[24] It is defined for a given sample as $(I^R - I^L)/(I^R + I^L)$, where I^R and I^L stand for the total scattered SHG intensity, either under R-polarized or L-polarized excitation, respectively. Due to the parity relation between the two mirror cases, such a parameter is directly associated with the SHG intensity difference between the two enantiomers under excitation by circularly polarized light of a given handedness. It is therefore adapted to account for the readout performance of the investigated chirality-encoded patterns. It is estimated by averaging the SHG signal from each array, taking into account all pixels of the scans corresponding to the emission from a given array. Under illumination by right-handed circular polarization, the average SHG signal from the right-enantiomer array amounts to 2300 ± 50 cts/s, to be compared to a slightly weaker emission from the nonchiral array, 1850 ± 50 cts/s, and an even weaker SHG from the left-enantiomer array, 1400 ± 30 cts/s. Under the left-handed polarization, the situation is opposite, the right-enantiomer emits 1380 ± 30 cts/s, compared to much stronger SHG emission from the left-enantiomer, 2050 ± 50 cts/s, and a moderate intermediate SHG intensity from the nonchiral array, 1900 ± 50 cts/s, close to the previous value for right-handed circular polarization. From the above numerical values, the SHG-CD equals 25 ± 2% for the right-enantiomer array and −15 ± 2% for the left-enantiomer array. These values are confirmed by additional measurements of the emission spectra, which are presented in the SI.

Apparently, the nonlinear chiroptical effect shows-up with different magnitudes for the two opposite enantiomers. We attribute the observed imbalance to a regular deviation from a perfect mirror symmetry between the two enantiomers, as a consequence of limited accuracy of the fabrication process. In particular, the distortions responsible for this effect may be related to nanoparticles getting in contact with each other, as investigated in more details in the SI. Some contribution of very bright hot spots at strongly defected nanostructures may also occur; however, such distortions are random, contributing with equal probability to SHG-CD of both enantiomers. Averaging of |SHG-CD| of both enantiomers gives 20 ± 7%, which corresponds to a total contrast of about 40%, when comparing the SHG intensity from the two opposite enantiomers irradiated either by L or by R polarization.

Building-up on this property, we switch from uniform arrays to a mixture of two different enantiomers forming a chirality-encoded "watermark". A pattern shaped after the capital letter "R" was chosen to indicate the R-polarized excitation, as in this case the right-enantiomers form the "R" letter, whereas the left-enantiomers constitute the background. Such a pattern may serve as a reliable test for the read-out performance, providing horizontal, vertical, diagonal, and rounded lines, as well as a separated "island" of opposite chirality. The thickness of a line in this pattern is between 3 and 4 individual enantiomers (1.5−2.0 μm), and the entire array has a size of 21 × 21, that is roughly 10 × 10 μm, as seen from the SEM image in Figure 2c. Figure 2d shows two SHG images, the first one obtained using R excitation, and the second one using L excitation. Here again, the chiroptical effect appears clearly: in the first case the "R" letter appears bright on a dark background, whereas in the second case the situation is reversed.

Additionally, the readability of the pattern under three different excitation wavelengths: 800, 850, and 900 nm, is compared in Figure 3. Averaged |SHG-CD| calculated at 800 and 900 nm is 15 ± 4 and 27 ± 5%, respectively, compared to previously determined 20 ± 7% at 850 nm. Despite higher |SHG-CD| magnitude of the SHG excited at 900 nm, larger inhomogeneity of the signal hampers the readability of the "watermark", making 850 nm a better wavelength for this purpose. These results can be explained in terms of the spectral location of specific localized plasmon resonance bands, to be discussed in the next section.

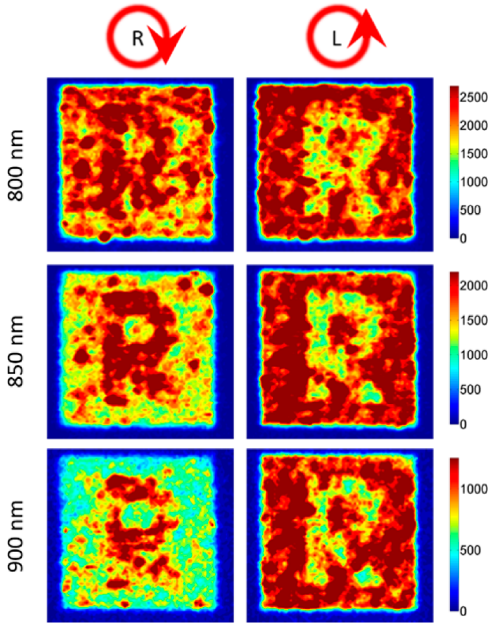

Figure 3. Comparison between SHG images of the chirality-encoded "watermark" for L- and R-circular polarizations, under different excitation wavelengths. Numbers on the color bars (on the right) indicate the SHG intensity in counts per second.

Linear Optical Regime: Measurements and Simulations. In order to better account for the above nonlinear optical results, we compare them with the behavior in the linear optical regime for the same nanostructures. We have investigated the spectral dependence of the extinction coefficient, using UV−vis spectroscopy with circularly polarized light (see SI for more details) and we also performed numerical simulations using the COMSOL Multiphysics software, based on the finite element method to solve Maxwell equations in the frequency domain. A realistic model of the sample was created, as shown in Figure 1. Optical properties of ITO were taken from the Sopra Material Database, whereas the properties of gold and chromium were based on the experimental data of Johnson and Christy.[36,37] An individual nanostructure consists of three equilateral triangular prisms of side-length 190 nm, surrounding a smaller prism of side length 55 nm at the center. The sharpness of cusps and edges is softened by introducing a finite curvature radius of 10 nm. Three larger prisms are arranged into a chiral pattern, with an apex-to-base gap equal 40 nm. The nanostructure is placed at the center of a spherical simulation space, enclosed by a perfectly matched layer (PML) of thickness $\lambda/2$ and of inner radius $\lambda/2$ + 250 nm. The nanostructure is irradiated by a normally incident, uniform, circularly polarized plane wave, which propagates from the air side toward the glass substrate. The scattered radiation is absorbed by the PML, and the electric field is constrained to decay to zero at the outermost boundaries of the simulation space.

Absorption and scattering cross sections are calculated separately for each studied wavelength of the incident light, using formulas given by Knight and Halas:[38] the absorption cross-section is calculated by integration of the resistive heating over the volume of the nanoparticles, whereas the scattering cross section is calculated by integration of the far-field over the upper hemisphere of a spherical enclosure of the nanostructure. In this last case, the integration accounts only for backscattering, because scattering in the forward direction contributes to the transmitted light and, therefore, tends to decrease the magnitude of the extinction measured in the UV−vis experiment.

Extinction spectra obtained in the UV−vis measurements are presented in Figure 4a, with the results obtained from numerical simulations shown in Figure 4b for comparison. Only two independent cases are to be considered: "case 1" corresponding to the right-enantiomer under R polarization (or its mirror counterpart: left-enantiomer under L polarization), and "case 2", when the right-enantiomer is irradiated by L-polarized light (or the mirror image of this situation). Both cases and their mirror images are illustrated in Figure 4c. In the plots of the experimental and theoretical spectra, the data corresponding to "case 1" are plotted in blue, whereas the data plotted in red are associated with "case 2".

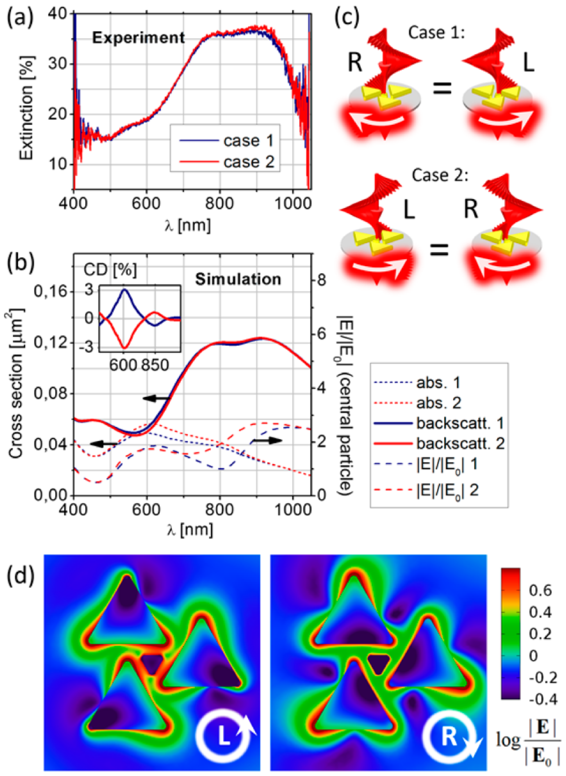

Figure 4. (a) UV−vis spectra of the right-enantiomer ("case 1", blue line) and the left-enantiomer ("case 2", red line), both measured using L-polarized light; (b) spectral dependence of the backscattering cross section (solid lines), absorption cross section (dotted lines), and the local field factor at the surface of the central nanoparticle (dashed lines), calculated by COMSOL; the inset shows the backscattering-CD spectrum; (c) illustration of the "case 1" and "case 2" configurations; (d) calculated electric field distribution at 850 nm in the left-enantiomer (cross section plane at the level of Cr−Au junction) under R polarization ("case 1", on the right) or L polarization ("case 2", on the left), plotted in logarithmic scale.

Calculated backscattering spectra (Figure 4b, solid lines) are very similar to the measured extinction spectra (Figure 4a), except for the small peak around 550 nm, which appears only in the calculated absorption spectrum (Figure 4b, dotted lines). Both measured extinction and calculated backscattering spectra evidence two strongly overlapping bands: one centered around 800 nm and a second one around 900 nm. These bands originate from the near-field coupling between triangular prisms, leading to hybridization of the dipolar plasmon mode of a single gold nanoprism into bonding and antibonding modes.[39] Weak separation of these bands arises, due to the limit put on the interaction, by the relatively large size of the gap between nanoparticles (estimated around 40 nm), as compared to the range of near-field interactions. These results can be compared with the calculated absorption and scattering spectra of a single small nanoparticle and a single nanoprism, as presented in the SI. Additionally, the effect of the distance between nanoprisms on the plasmon hybridization is also investigated in the SI in a separate section.

The 850 nm wavelength, which optimizes the quality of SHG images, is falling exactly in-between these two bands. Some relatively faint chiroptical effect in the calculated backscattering, showing up as a difference between the red and blue curves in the spectrum, is observed within this spectral region. The magnitude of this effect can be estimated by analogy with the SHG-CD factor by identifying I^R and I^L, with the scattered intensity now at the fundamental frequency. At 850 nm, this backscattering-CD is predicted to be less than 1% (see Figure 4b, inset), whereas at 800 and 900 nm (close to the backscattering maxima), it almost drops down to zero. This could be the cause of the deterioration of the SHG images at the fundamental wavelengths of 800 and 900 nm. Apart from a lower CD in the linear regime, these wavelengths are also closer to the plasmon resonance peaks. This may be associated with a more resonant character of light−matter interactions, resulting in stronger stimulation of defect-induced hot spots that are prone to decrease the "watermark" image readability.

The chiroptical effect is slightly more pronounced at wavelengths around 600 nm, backscattering-CD reaching 3% (inset of Figure 4b), which gives a total contrast between the two enantiomers of 6%. Therefore, one can predict that reading the "watermark" using dark-field microscopy with an excitation around 600 nm would be possible; however, in such case, the contrast would be much lower than for SHG microscopy, requiring some additional postprocessing of the obtained images. Other linear optical techniques, such as transmission measurements using circular dichroism imaging microscopy (CDIM),[40] would probably prove inadequate, due to opposite chiroptical effects of the absorption and backscattering (see Figure 4b), resulting in a vanishingly small extinction-CD.

The effect of chirality is more visible in the spectral dependence of the average local field enhancement at the surface of the central nanoparticle (Figure 4b, dashed lines). It results from a significant sensitivity of the location of plasmonic hot spots to the incident handedness, which is shown in Figure 4d: in "case 1", the hot spots are moved to the outermost corners of the three gold prisms (Figure 4d, on the right), whereas in "case 2", the electric field concentrates at the center of the nanostructure, around the central nanoparticle (Figure 4d, on the left). One can presume that the spatial distribution of the second order nonlinear polarization density will, to some extent, follow the distribution of hot spots at the fundamental frequency. This will affect the far-field SHG radiation pattern:

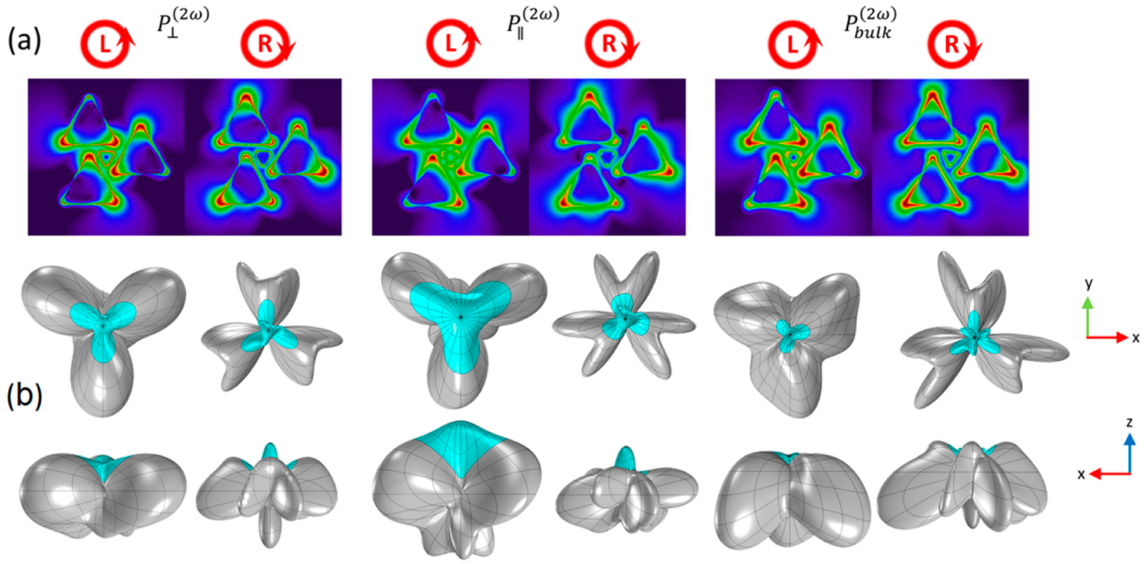

Figure 5. SHG simulation results: (a) electric field distribution at the second-harmonic frequency (plotted in logarithmic scale); (b) 3D polar plots of the far-field SHG intensity pattern. Data are plotted separately for each microscopic contribution (surface normal on the left, surface tangential in the middle, bulk on the right), under incident circular polarizations of different handedness (as indicated). 3D polar plots are shown in top-view (upper line, viewing direction normal to *xy* plane) and in side-view (lower line, viewing direction normal to the *zx* plane).

in "case 1", the sources of the scattered harmonic radiation will be separated by a distance of ∼300−400 nm, thus, weakening the buildup of constructive interferences in the far-field, whereas in "case 2", the sources will concentrate within a small volume around the nanostructure center, resulting in a more coherent SHG backscattering.

SHG Scattering Simulations. In order to confirm the conjectured mechanism for the SHG chiroptical effect, we performed numerical simulations of the SHG scattering at a single wavelength 850 nm, following the two-step modeling procedure in refs 17 and 18. In this computational approach, the scattered radiation at the harmonic frequency is derived from the spatial distribution of nonlinear currents generated by the second-order polarization. The latter one is obtained in the first simulation step (at fundamental frequency) from three independent microscopic contributions to the nonlinear optical susceptibility of gold: surface normal ($P_{\perp}^{(2\omega)}$), surface tangential ($P_{\parallel}^{(2\omega)}$), and bulk ($P_{\text{bulk}}^{(2\omega)}$) induced harmonic polarizations. These contributions are accounted for separately, assuming Rudnick-Stern parameters *a*, *b*, and *d* equal 1. The values of these parameters affect only the absolute SHG efficiency, having no qualitative effect on the far-field radiation pattern (hence, no quantitative effect on SHG-CD), which is explained in more details in the SI. The fundamental electric field is defined as a uniform circularly polarized plane wave, which is a coarse approximation of the focused laser beam used in our experiment. The collected SHG intensity is calculated by integration of the SHG far-field pattern over the acceptance cone of the objective. More details on the SHG simulations can be found in the SI.

Both the near-field distributions and the far-field intensity patterns at second-harmonic frequency, obtained separately for each microscopic contribution on the example of the left-enantiomer are subsequently presented in Figure 5. As expected, the SHG field distribution (Figure 5a) responds to the incident polarization handedness in a similar manner as the electric field at fundamental frequency: in the left-enantiomer, under L polarization, the second-harmonic hot spots tend to localize in the center of the nanostructure, whereas under R polarization, they tend to withdraw to the outer corners. The 3D polar plots of the far-field (Figure 5b) clearly show that, in the first situation, the SHG radiation builds-up via constructive interferences in a more efficient way than in the second case.

However, what actually contributes to the detected SHG intensity is the fraction of the scattered SHG that can be eventually collected by the objective. This fraction is highlighted in the polar plots in light blue color. It shows that in all cases, most of the SHG radiation is scattered sideways, leaving only a small amount of SHG for backward emission. In other words, it is only a small portion of the total emitted SHG which is detected during the experiment, leaving therefore a margin for increasing the efficiency of our experiments. One can indeed expect that improving the SHG collection efficiency will further significantly increase the quality of the obtained results, which is one of the current goals of our ongoing research. Integration of the $|\mathbf{E}_{\text{far}}^{(2\omega)}|^2$ contained within the objective acceptance cone gives the overall measured SHG intensity, which gives theoretical SHG-CD of −16% for the surface normal, −37% for the surface tangential, and +7% for the bulk SHG contribution (where the ± sign is associated with the applied SHG-CD definition). In the latter case, the chiroptical effect is opposite with respect to the surface contributions. These results are in agreement with experimental |SHG-CD| values equal in the range of 20%, taking into account that the resultant SHG originates from a coherent mixture of the discussed microscopic sources. In the case of gold, the surface normal contribution is commonly assumed to be dominant over the two other tangential and bulk sources.[18,31,41] Among them, the bulk contribution may be more or less important, depending on whether the metal is formed as a thin film or as a nanoparticle. Comparison of the above theoretical results with the experimental ones allows to infer that in our case, the SHG signal originates mainly from surface normal currents, as the obtained |SHG-CD| for this kind of nonlinear sources is very close to the measured one. An additional increase of this factor may be then attributed to a coherent interplay between strongly positive surface tangential and negative bulk contribution, involving the interference of these sources with the dominant surface normal contribution.

Numerical simulations can be applied to investigate theoretically the influence of various factors on the measured SHG-CD, such as resulting from geometrical modifications. Dependence on the distance between the nanoprisms, which determines the strength of the plasmonic near-field interactions, and the influence of the small central nanoparticle are addressed in the SI. It is found that indeed the presence of the central nanoparticle is crucial toward the SHG-CD efficiency: without the nanoparticle, the value of |SHG-CD|, originating from surface normal contribution, drops down from 16 to 6%, whereas increasing the size of the nanoparticle from 55 to 100 nm is boosting the |SHG-CD| up to 50%. In another section of the SI, we present the results of simulations for a defective geometry, whereby the smaller central nanoparticle gets in contact with one of the larger nanoprisms. Such defects are found to increase the |SHG-CD| originating from surface normal contribution up to 33%, which provides a plausible explanation to the apparent asymmetry of the SHG-CD magnitude between the two enantiomers due to different fraction of the defected elements appearing in the enantiomer arrays.

CONCLUSIONS

Strong chiroptical effects in the backscattered SHG from 2D chiral arrangements of gold nanoprisms have been measured using nonlinear microscopy and confirmed by numerical simulations. The triangular motif of the investigated nanostructures, provide efficient dipole-allowed SHG due to lack of inversion symmetry, as well as sharp corners prone to large local field enhancements. Because the investigated nanostructures are built from nonchiral elements (triangular nanoprisms), the observed chiroptical effects can be attributed to the plasmonic near-field coupling between the nanostructures. Subwavelength dimensions of the individual enantiomers enable fabrication of a subdiffraction-limited chirality-encoded pattern, which can be efficiently read-out by SHG imaging with circularly polarized excitation. It is found that the optimal excitation wavelength for such imaging lies in between two plasmon resonance bands resulting from the sp2-like hybridization of the dipolar plasmon modes of individual nanoprisms. These results open the perspectives of a new class of superchiral metamaterials, composed of interacting nanoparticles making chiral nonlinear “meta-molecules”, where chirality originates from the mutual arrangement and interparticle plasmonic interactions and not from the shape of nanoparticles. Such meta-molecular engineering approach provides a strong SHG chiroptical effect even at the level of 2D chiral arrangement. Moreover, the strength of these interactions can be controlled by the size of the gaps between the nanoparticles. The nanostructure geometry could be further optimized so as to minimize linear circular dichroism while maximizing the SHG chiroptical efficiency. Such optimized “meta-molecules” could serve as “meta-molecular” building blocks toward a new type of “watermarks”, which could be read-out only by way of a sophisticated nonlinear microscopy setup with circular polarizations.

ASSOCIATED CONTENT

Ⓢ Supporting Information

Additional results including experimentally measured emission spectra, computed optical properties of individual nanoparticles, SEM images of structural defects, and theoretical analysis of their influence on the SHG-CD, as well as results of numerical simulations performed for modified geometries, including nanostructures without central nanoparticle, with central nanoparticle of larger size, and with various sizes of the interparticle gap. It also contains a detailed description of methods used here, namely, nanostructure fabrication, UV−vis characterization, and SHG simulations, with an alternative simulation method for the surface normal contribution. The Supporting Information is available free of charge on the ACS Publications website at DOI: 10.1021/acsphotonics.5b00090.

AUTHOR INFORMATION

Corresponding Author

*E-mail: radoslaw.kolkowski@pwr.edu.pl.

Notes

The authors declare no competing financial interest.

ACKNOWLEDGMENTS

This work was supported by the European Regional Development Fund - FESR of P.O.R. Campania 2007-2013 - Call Innovation Window, Project title: Kit for Brucella Abortus e B. Melitensis nano-BIosensing RApid detection (AMBRA). We thank Dr. R. Capasso and Dr. E. Bobeico for their support in the fabrication process of the nanostructures. The work of R.K. on numerical simulations carried out in Wroclaw was supported by the Foundation for Polish Science under the Welcome Project (led by Prof. M. Samoc) and The National Science Centre, Project DEC-2012/04/M/ST5/00340.

REFERENCES

(1) Vance, F. W.; Lemon, B. I.; Hupp, J. T. Enormous Hyper-Rayleigh Scattering from Nanocrystalline Gold Particle Suspensions. *J. Phys. Chem. B* **1998**, *102*, 10091−10093.

(2) Russier-Antoine, I.; Jonin, C.; Nappa, J.; Bénichou, E.; Brevet, P. F. Wavelength Dependence of the Hyper Rayleigh Scattering Response from Gold Nanoparticles. *J. Chem. Phys.* **2004**, *120*, 10748−52.

(3) Johnson, R. C.; Li, J.; Hupp, J. T.; Schatz, G. C. Hyper-Rayleigh Scattering Studies of Silver, Copper, and Platinum Nanoparticle Suspensions. *Chem. Phys. Lett.* **2002**, *356*, 534−540.

(4) Jin, R. J.; Jureller, J. E.; Kim, H. Y.; Scherer, N. F. Correlating Second Harmonic Optical Responses of Single Ag Nanoparticles with Morphology. *J. Am. Chem. Soc.* **2005**, *127*, 12482−12483.

(5) Butet, J.; Duboisset, J.; Bachelier, G.; Russier-Antoine, I.; Benichou, E.; Jonin, C.; Brevet, P. F. Optical Second Harmonic Generation of Single Metallic Nanoparticles Embedded in a Homogeneous Medium. *Nano Lett.* **2010**, *10*, 1717−172.

(6) Salomon, A.; Zielinski, M.; Kolkowski, R.; Zyss, J.; Prior, Y. Size and Shape Resonances in Second Harmonic Generation from Silver Nanocavities. *J. Phys. Chem. C* **2013**, *117*, 22377−22382.

(7) Valev, V. K. Characterization of Nanostructured Plasmonic Surfaces with Second Harmonic Generation. *Langmuir* **2012**, *28*, 15454−15471.

(8) Nappa, J.; Revillod, G.; Russier-Antoine, I.; Benichou, E.; Jonin, C.; Brevet, P. F. Electric Dipole Origin of the Second Harmonic Generation of Small Metallic Particles. *Phys. Rev. B* **2005**, *71*, 165407.

(9) Kujala, S.; Canfield, B. K.; Kauranen, M.; Svirko, Y.; Turunen, J. Multipole Interference in the Second-Harmonic Optical Radiation from Gold Nanoparticles. *Phys. Rev. Lett.* **2007**, *98*, 167403.

(10) Czaplicki, R.; Zdanowicz, M.; Koskinen, K.; Laukkanen, J.; Kuittinen, M.; Kauranen, M. Dipole Limit in Second-Harmonic Generation from Arrays of Gold Nanoparticles. *Opt. Express* **2011**, *19*, 26866−26871.

(11) Salomon, A.; Prior, Y.; Fedoruk, M.; Feldmann, J.; Kolkowski, R.; Zyss, J. Plasmonic Coupling between Metallic Nanocavities. *J. Opt.* **2014**, *16*, 114012.

(12) Kolkowski, R.; Szeszko, J.; Dwir, B.; Kapon, E.; Zyss, J. Effects of Surface Plasmon Polariton-Mediated Interactions on Second Harmonic Generation from Assemblies of Pyramidal Metallic Nano-Cavities. *Opt. Express* **2014**, *22*, 30592−30606.

(13) Butet, J.; Russier-Antoine, I.; Jonin, C.; Lascoux, N.; Benichou, E.; Brevet, P. F. Sensing with Multipolar Second Harmonic Generation from Spherical Metallic Nanoparticles. *Nano Lett.* **2012**, *12*, 1697−1701.

(14) Butet, J.; Thyagarajan, K.; Martin, O. J. F. Ultrasensitive Optical Shape Characterization of Gold Nanoantennas Using Second Harmonic Generation. *Nano Lett.* **2013**, *13*, 1787−1792.

(15) Butet, J.; Martin, O. J. F. Nonlinear Plasmonic Nanorulers. *ACS Nano* **2014**, *8*, 4931−4939.

(16) Bautista, G.; Huttunen, M. J.; Makitalo, J.; Kontio, J. M.; Simonen, J.; Kauranen, M. Second-Harmonic Generation Imaging of Metal Nano-Objects with Cylindrical Vector Beams. *Nano Lett.* **2012**, *12*, 3207−3212.

(17) Bachelier, G.; Russier-Antoine, I.; Benichou, E.; Jonin, C.; Brevet, P. F. Multipolar Second-Harmonic Generation in Noble Metal Nanoparticles. *J. Opt. Soc. Am. B* **2008**, *25*, 955−960.

(18) Bachelier, G.; Butet, J.; Russier-Antoine, I.; Jonin, C.; Benichou, E.; Brevet, P. F. Origin of Optical Second-Harmonic Generation in Spherical Gold Nanoparticles: Local Surface and Nonlocal Bulk Contributions. *Phys. Rev. B* **2010**, *82*, 235403.

(19) Ginzburg, P.; Krasavin, A. V.; Wurtz, G. A.; Zayats, A. V. Nonperturbative Hydrodynamic Model for Multiple Harmonics Generation in Metallic Nanostructures. *ACS Photonics* **2015**, *2*, 8−13.

(20) Papakostas, A.; Potts, A.; Bagnall, D. M.; Prosvirnin, S. L.; Coles, H. J.; Zheludev, N. I. Optical Manifestations of Planar Chirality. *Phys. Rev. Lett.* **2003**, *90*, 107404.

(21) Kuwata-Gonokami, M.; Saito, N.; Ino, Y.; Kauranen, M.; Jefimovs, K.; Vallius, T.; Turunen, J.; Svirko, Y. Giant Optical Activity in Quasi-Two-Dimensional Planar Nanostructures. *Phys. Rev. Lett.* **2005**, *95*, 227401.

(22) Valev, V. K.; Silhanek, A. V.; Smisdom, N.; De Clercq, B.; Gillijns, W.; Aktsipetrov, O. A.; Ameloot, M.; Moshchalkov, V. V.; Verbiest, T. Linearly Polarized Second Harmonic Generation Microscopy Reveals Chirality. *Opt. Express* **2010**, *18*, 8286−8293.

(23) Valev, V. K.; Silhanek, A. V.; Jeyaram, Y.; Denkova, D.; De Clercq, B.; Petkov, V.; Zheng, X.; Volskiy, V.; Gillijns, W.; Vandenbosch, G. A. E.; Aktsipetrov, O. A.; Ameloot, M.; Moshchalkov, V. V.; Verbiest, T. Hotspot Decorations Map Plasmonic Patterns with the Resolution of Scanning Probe Techniques. *Phys. Rev. Lett.* **2011**, *106*, 226803.

(24) Valev, V. K.; Baumberg, J. J.; De Clercq, B.; Braz, N.; Zheng, X.; Osley, E. J.; Vandendriessche, S.; Hojeij, M.; Blejean, C.; Mertens, J.; Biris, C. G.; Volskiy, V.; Ameloot, M.; Ekinci, Y.; Vandenbosch, G. A. E.; Warburton, P. A.; Moshchalkov, V. V.; Panoiu, N. C.; Verbiest, T. Nonlinear Superchiral Meta-Surfaces: Tuning Chirality and Disentangling Non-Reciprocity at the Nanoscale. *Adv. Mater.* **2014**, *26*, 4074−4081.

(25) Toyoda, K.; Miyamoto, K.; Aoki, N.; Morita, R.; Omatsu, T. Using Optical Vortex To Control the Chirality of Twisted Metal Nanostructures. *Nano Lett.* **2012**, *12*, 3645−3649.

(26) Kuzyk, A.; Schreiber, R.; Fan, Z.; Pardatscher, G.; Roller, E. M.; Högele, A.; Simmel, F. C.; Govorov, A. O.; Liedl, T. DNA-Based Self-Assembly of Chiral Plasmonic Nanostructures with Tailored Optical Response. *Nature* **2012**, *483*, 311−314.

(27) Esposito, M.; Tasco, V.; Cuscuna, M.; Todisco, F.; Benedetti, A.; Tarantini, I.; De Giorgi, M.; Sanvitto, D.; Passaseo, A. Nanoscale 3D Chiral Plasmonic Helices with Circular Dichroism at Visible Frequencies. *ACS Photonics* **2015**, *2*, 105−114.

(28) Frank, B.; Yin, X.; Schaferling, M.; Zhao, J.; Hein, S. M.; Braun, P. V.; Giessen, H. Large-Area 3D Chiral Plasmonic Structures. *ACS Nano* **2013**, *7*, 6321−6329.

(29) Dhenaut, C.; Ledoux, I.; Samuel, I. D. W.; Zyss, J.; Bourgault, M.; Le Bozec, H. Chiral Metal Complexes with Large Octupolar Optical Nonlinearities. *Nature* **1995**, *374*, 339−342.

(30) Zyss, J. Molecular Engineering Implications of Rotational Invariance in Quadratic Nonlinear Optics: From Dipolar to Octupolar Molecules and Materials. *J. Chem. Phys.* **1993**, *98*, 6583−6599.

(31) Butet, J.; Bachelier, G.; Russier-Antoine, I.; Jonin, C.; Benichou, E.; Brevet, P.-F. Interference between Selected Dipoles and Octupoles in the Optical Second-Harmonic Generation from Spherical Gold Nanoparticles. *Phys. Rev. Lett.* **2010**, *105*, 077401.

(32) Stockman, M. I.; Li, K.; Brasselet, S.; Zyss, J. Octupolar Metal Nanoparticles As Optically Driven, Coherently Controlled Nanorotors. *Chem. Phys. Lett.* **2006**, *433*, 130−135.

(33) Hentschel, M.; Schäferling, M.; Weiss, T.; Liu, N.; Giessen, H. Three-Dimensional Chiral Plasmonic Oligomers. *Nano Lett.* **2012**, *12*, 2542−2547.

(34) Hentschel, M.; Schäferling, M.; Metzger, B.; Giessen, H. Plasmonic Diastereomers: Adding up Chiral Centers. *Nano Lett.* **2013**, *13*, 600−606.

(35) Li, K.; Stockman, M. I.; Bergman, D. J. Self-Similar Chain of Metal Nanospheres as an Efficient Nanolens. *Phys. Rev. Lett.* **2003**, *91*, 227402.

(36) Johnson, P. B.; Christy, R. W. Optical Constants of the Noble Metals. *Phys. Rev. B* **1972**, *6*, 4370−4379.

(37) Johnson, P. B.; Christy, R. W. Optical Constants of Transition Metals: Ti, V, Cr, Mn, Fe, Co, Ni, and Pd. *Phys. Rev. B* **1974**, *9*, 5056−5070.

(38) Knight, M. W.; Halas, N. J. Nanoshells to Nanoeggs to Nanocups: Optical Properties of Reduced Symmetry Core-Shell Nanoparticles beyond the Quasistatic Limit. *New J. Phys.* **2008**, 10.

(39) Halas, N. J.; Lal, S.; Chang, W. S.; Link, S.; Nordlander, P. Plasmons in Strongly Coupled Metallic Nanostructures. *Chem. Rev.* **2011**, *111*, 3913−3961.

(40) Claborn, K.; Puklin-Faucher, E.; Kurimoto, M.; Kaminsky, W.; Kahr, B. Circular Dichroism Imaging Microscopy: Application to Enantiomorphous Twinning in Biaxial Crystals of 1,8-Dihydroxyanthraquinone. *J. Am. Chem. Soc.* **2003**, *125*, 14825−14831.

(41) Wang, F. X.; Rodríguez, F. J.; Albers, W. M.; Ahorinta, R.; Sipe, J. E.; Kauranen, M. Surface and Bulk Contributions to the Second-Order Nonlinear Optical Response of a Gold Film. *Phys. Rev. B* **2009**, *80*, 233402.